Suppression of wall reflections in PIV images over rough walls

W. Abu Rowin[1,*], M. Abdelkader[1], A. Ramani[1], P. Manovski[1,2], N. Hutchins[1]

1: Dept. of Mechanical Engineering, University of Melbourne, Victoria 3010, Australia
2: Defence Science and Technology Group, Melbourne VIC 3207, Australia
*Corresponding author: waburowin@unimelb.edu.au

Keywords: Rough walls, laser reflection, near-wall velocity measurements

ABSTRACT

Wall reflections in particle image velocimetry (PIV) measurements is one of the limiting factors in obtaining velocity information in the vicinity of rough walls. This work tests two different techniques to suppress wall reflections for time-resolved, two-dimensional particle tracking velocimetry (2D-PTV) and stereoscopic-PIV (stereo-PIV). The 2D-PTV was performed for a turbulent boundary layer developed on a rough wall in a water towing tank facility. To measure velocity in the vicinity of the rough wall, the near-wall region on the viewing window was covered with tinted papers to mitigate the wall reflection and maintain a visible reference plane of the towed w all. Three layers of tinted paper with 65% light blockage were found to be the optimum combination to reduce wall reflections while allowing for particle detection just above the visible roughness features. Using this technique allowed detection of particles at a wall-normal distance of approximately 300 µm ($\sim$ 10 wall units) from the roughness valleys for an imaging system with $\sim$ 1 m standoff distance. To suppress the wall refection for the stereo-PIV over a rough wall performed in a wind tunnel, the roughness is coated with fluorescent paint to shift the reflected light to a higher wavelength. A narrow band-pass filter was then used on the imaging lenses, allowing only particle images to be recorded while extinguishing the majority of the reflected laser light from the s urface. Three different fluorescent paints were evaluated. Rhodamine 6G was found to have the best performance for suppressing wall and background reflections. Reliable velocity measurements with this technique were obtained up to 500 µm ($\sim$ 5.0 wall units) from the roughness valleys. The same technique was also successfully used with stereo-PIV to detect the secondary motions within riblet valleys.

1. Introduction

In the past few decades, there has been an increased interest in understanding the mechanisms by which drag increasing and drag reducing surfaces affect the flow in the vicinity of the walls. For example, several mechanisms have been suggested for why the drag reducing capability of riblets diminishes at higher viscous-scaled riblet spacing, including lodgement of near-wall vortices within the riblet valleys (Choi et al., 1993), the formation of secondary flows (Goldstein &

Tuan, 1998) and a Kelvin-Helmholtz instability (Garcia-Mayoral & Jimenez, 2011). Likewise, the breakdown of drag reduction on superhydrophobic surfaces, the depletion of the air plastron over the superhydrophobic surfaces has been proposed (Rothstein, 2010). To obtain answers for these undetermined mechanisms velocity measurements very close to the wall are required.

Despite the importance of such velocity measurements very close to the rough walls (or walls in general), there is typically a lack of flow information in this region. This lack is associated with the limitations and challenges of deploying velocity-measurement instruments very close to the wall. For instance, hot-wire anemometers suffer from additional heat losses to the wall and complications of traversing or placing the wire very close to the wall. The former limitation results in an increase of hot-wire anemometer output beyond the value corresponding to the local velocity (Khoo et al., 2000), while the latter results in breaking the wire or damaging the probe. As a single point measurement, hot-wire measurements are also not particularly well-suited to measuring the secondary flows or dispersive stresses that form near to textured surfaces. Particle image velocimetry (PIV) is also typically limited for near-wall velocity measurements due to the laser reflection from the wall, which is sometimes aggravated by the lack of seeding close to the wall. Though this latter issue is typically resolved by increasing the seeding density or injecting particles just upstream of the field of view (FOV) (Talapatra & Katz, 2012). The issue of reflected light, however, remains a significant barrier to near-wall PIV measurements over textured surfaces.

Several attempts have been made to overcome the limitation of near-wall velocity measurements for the different velocity-measurement instruments. For hot-wire anemometers, schemes and methods are introduced to correct the corrupted data due to the heat loss near the wall (Bhatia et al., 1982). The laser reflection from the wall could also be suppressed by using shadowgraphy or directing the laser sheet parallel to the top wall as in Abu Rowin et al. (2017), although this precludes the possibility of making measurements within the roughness canopy. However, for cases where the laser sheet is illuminated perpendicular to the rough wall, the intensity of the reflected light from the roughness features can be an order of magnitude larger than the tracer particle images. The use of mirror-polished or glass surfaces can also minimise the wall reflection for PIV images (C. Kähler, 2009), but this technique is only valid for flat surfaces as the roughness features would still scatter the light when illuminated with a light sheet. In situations where the laser reflection from the wall does not saturate the cameras, the reflection can be treated as background reflection and omitted by subtracting a reference intensity map or minimum intensity map from the ensemble of images (Gui, 1997; Wereley et al., 2002). If the glare from the rough wall does not extend in the wall-normal direction, and sufficient contrast exists between the particles and the laser reflection, the FOV can then be adjusted just above the reflection region as in the stereo-PIV over streamwise strips of Vanderwel & Ganapathisubramani (2015) and Wangsawijaya et al. (2020). Similarly, the highly illuminated region could be blocked or masked physically from the camera view with an opaque sheet. Both methods, however, do not allow for measurements very close to the wall or within the roughness canopy. They also lead to the loss of a reference wall location as it is not captured in the images.

For some water flows, the laser reflection issue is suppressed by seeding the flow facility with particles that emit light at a wavelength different from the illuminated light. Then the cameras are equipped with the band- or long-pass filters to only pass the light emitted by the particles. For example, fluorescent particles absorb light from Nd: YAG or Nd: YLF at a wavelength $\lambda = 532\,\mathrm{nm}$ and emit light with a wavelength of $\lambda \gtrsim 570\,\mathrm{nm}$. Filters with a wavelength range larger than 545 nm are then mounted on the cameras. This technique was used for planar PIV of Meinhart et al. (1999), stereo-PIV of Dreyer et al. (2014) and three-dimensional particle tracking velocimetry of Rowin & Ghaemi (2019). This technique is not feasible for air flows and large-scale water facilities due to the density and high cost of the fluorescent particles, respectively. It is common practice to coat the roughness with matt black paint in those cases. However, this method is only sufficient for low magnification PIV as the paint still produces reflections, which might still saturate the images for high magnification near-wall PIV measurements. Alternatively, fluorescent paint can be applied to the surface to change the reflected light's wavelength with camera filters fitted to screen the wall refection and only allow the scattered light from the tracers. This technique has been adopted in several low magnification smooth wall measurements for example Depardon et al. (2005); Palmer et al. (2012); Eboibi et al. (2014); Hickling et al. (2019). This technique has not been tested for velocity measurements near the roughness crest and within the canopy.

In the present study, PIV measurements in near vicinity of rough walls are attempted with different laser reflection mitigation techniques. First, a novel surface masking technique to reduce the surface reflection is tested for time-resolved 2D-PTV measurements over a rough wall in a tow tank facility. Second, three fluorescent paints are tested to mitigate surface reflection using a stereo-PIV system in a wind tunnel for velocity measurement in the vicinity of a rough wall. In the final experiment, as a further proof of concept, the same mitigation technique for the stereo-PIV is used for preliminary velocity measurements above and within the valleys of drag increasing trapezoidal riblets.

2. Laser reflection mitigation for 2D-PTV

In this section, laser reflection mitigation is discussed for time-resolved 2D-PTV of a turbulent boundary layer developed on rough walls. Section 2.1 describes the experimental setup, the time-resolved 2D-PTV and details of the machined roughness. Section 2.2 details the method used to mitigate wall reflections. Lastly instantaneous velocity fields and mean profiles after implementing the wall reflection mitigation are presented in Section 2.3.

2.1. Experimental apparatus and procedures

The experiments are conducted in a 60 m long 2 m wide and 1.8 m tall tow tank facility in the Michell Laboratory at the University of Melbourne, see figure 1. The tank has a 5.0 m long flat plate with an eliptical leading edge that is towed at constant speed of $U_w = 0.87\,\mathrm{ms}^{-1}$. Five cen-

timetre thick glass windows on the tank side wall at 21 m from the upstream edge of the tank provide optical access. Two side-by-side PCO Dimax HS4 high-speed cameras, each with a resolution of 2016×2016 pixels^2 (12-bit CMOS), are synchronized with the laser at a 1 kHz frame rate. Each camera is equipped with Tamron 180 mm macro lens at $f/3.5$, resulting in a digital resolution of ≈ 0.48 mm/pix and a magnification of ≈ 0.17. The two camera FOVs overlap with ≈ 15 mm ($\sim 17\%$), reaching a total FOV of 170×85 mm^2 in the streamwise and wall-normal directions $(x \times z)$. The combined FOV is illuminated with a 100 mJ/pulse dual-head Nd: YLF laser (Photonics DM20-527) with laser sheet thickness of ≈ 2.5 mm in the spanwise (y) direction as measured with burn paper. The laser, cameras and automated traversing carriage are synchronized with Stanford Research Systems (SRS DG645) pulse generator, where 5,000 images are recorded over 4.5 m of the moving plate, with one image recorded every ≈ 0.91 mm that the plate traverses in the $x-$direction. Since the images are recorded at different x locations along the towed plate, 100 runs are performed to achieve convergence of statistical quantities (500,000 images in total). The tank is seeded with glass silver-coated particles with an average particles' diameter of 10 µm.

The measurements are carried out over an irregular, three-dimensional roughness topography which is generated numerically using a roughness generation algorithm (Jelly & Busse, 2019). The numerical tile (which has dimensions of 300×300 mm^2 and periodic boundaries) is physically reproduced using an in-house CNC router from acetal co-polymer sheets. The physical tiles have dimensions of 900×900 mm^2 (i.e. a 3×3 grid of the numerical tile). Five tiles are mounted on the bottom side of the moving plate covering 4.5 m in the *x*-direction. The rough surface is Gaussian (skewness ~ 0), with a mean-peak-to-valley height of 3 mm. A sample of the roughness heightmap from the numerical tile is shown in figure 1(*b*).

2.2. Reflection suppression

Since the laser is illuminated perpendicular to the rough wall, a strong reflection saturates the recorded image, as shown in the raw image in figure2(*a*). The intensity of the wall reflection is an order of magnitude higher than the intensity of the particles. Since the towed plate has some wall-normal motion (≈ 0.5 mm) as the towing carriage moves along the rails, using an opaque masking sheet to fully extinguish the reflected light is not practical as it is necessary to detect the instantaneous wall position from the images. Using fluorescent particles is also not practical and not cost effective owing to the large volume of the water flume of $\sim 220,000$ liters. For those reasons, a single sheet of tinted paper (Pillar, WF092GT) with 65% light blockage is placed on the window in front of the cameras' view to reduce the wall reflection, as shown in figure 1(*c*). The distance from the lens to the tinted paper is ≈ 50 mm and from the tinted paper to the imaging plane is ~ 930 mm. The resulted particle image from this configuration is shown in figure 2(*b*) and it is clear that there is a substantial drop in the wall reflection compared with figure 2(*a*). However, the wall reflection is still limiting the visibility of the particles in the near-wall region. Three layers of tinted paper were then used on the window to further block the wall reflections. A sample of the raw particles images with three layers of tinted paper is shown in figure 2(*c*). As can be

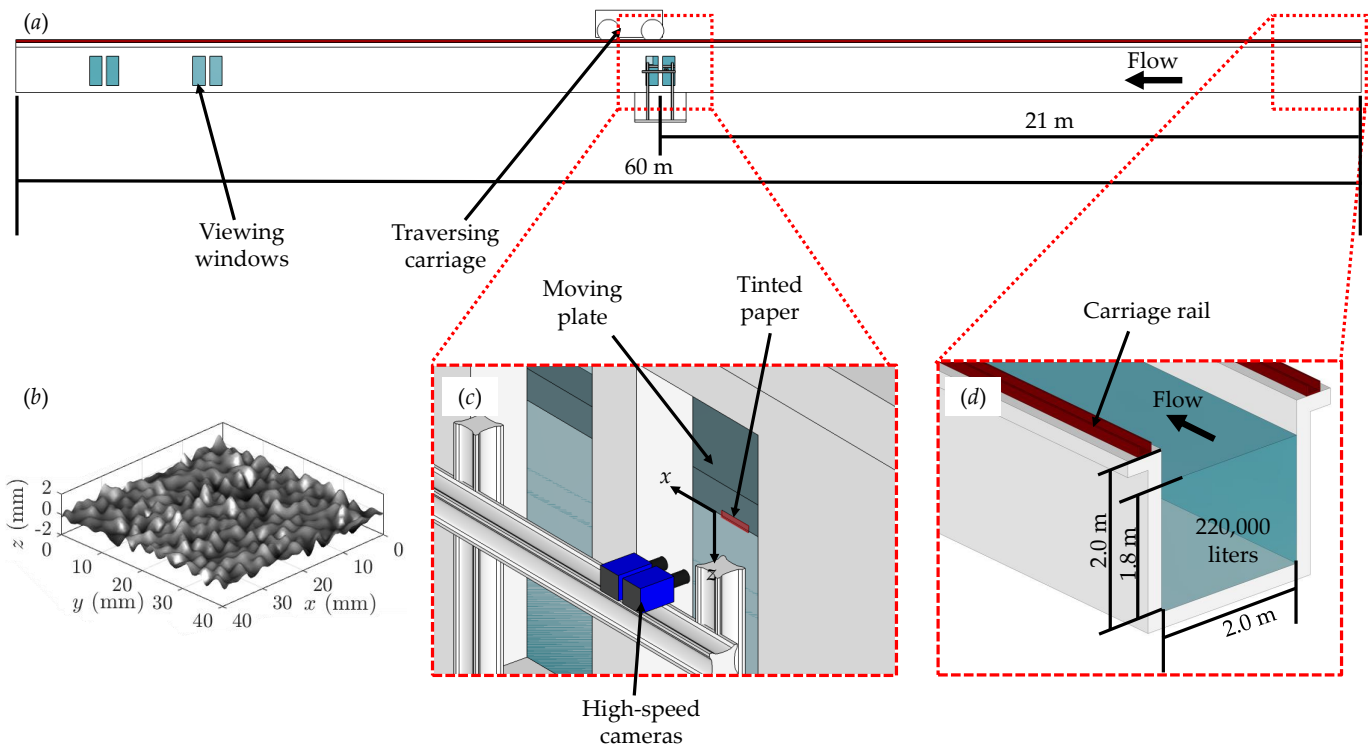

Figure 1. (*a*) a side view showing the tow tank, traversing carriage and the PIV system. (*b*) a sample of the irregular, three-dimensional roughness used for the experiments with the shading from black to white indicating the roughness height, $k = -2 - 2\,\mathrm{mm}$ (note: the z-axis has been scaled $2:1$ for clarity). (*c*) a close view showing the two-camera configuration and the tinted paper placement on the view window. (*d*) a view illustrating the dimensions of the tow tank.

seen, although the wall reflection is significantly suppressed, the wall location can still be detected with the observation of the roughness peaks. However, the light emitted by the particles is also significantly suppressed in this case. Finally, the three layers of tinted paper are placed to only cover the wall region, as shown by a red dashed line in figure 2(*d*). As illustrated, the particles are still visible up to the roughness features while the wall reflection is suppressed.

2.3. Results of 2D-PTV over a rough wall

The time-resolved images of the final case are processed using 2D-PTV algorithm in DaVis 10.2. Images of the two cameras are stitched using a mapping function obtained from a two-dimensional calibration target. The signal-to-noise ratio is improved by subtracting the minimum intensity of the ensemble of images. Firstly, ensemble of correlations of the images is estimated to serve as an initial velocity predictor. To reduce erroneous particle trajectories, particles with diameters less than 3 pixels and larger than 20 pixels are discarded. Trajectories shorter than five times-steps (particles detected in less than five consecutive images) are also removed. Particles are detected as close as $z \lesssim 300\,\mu\text{m}$ (≈ 10 wall units) from the wall. A sample of instantaneous streamwise, u, and wall-normal velocity, w, at $x = 1.48\,\text{m}$ from the moving plate leading edge is shown in figure 3(*a* and *b*), respectively. Here the plate is moving from right-to-left at $U_w = 0.87\,\text{ms}^{-1}$ while the flow is stationary. Thus, the negative values of u in figure 3(*a*) indicate displacement towards the left. At this streamwise location, the friction velocity estimated from the Clauser method is $U_\tau = 0.0474\,\text{ms}^{-1}$, corresponding to friction Reynolds number $Re_\tau = \delta U_\tau/\nu = 1721$, where $\delta = 39.7\,\text{mm}$ is the boundary layer thickness, which grows with increasing x along the moving plate, and ν is the kinematic viscosity. The velocity in figure 3 is obtained from averaging the data over $1.5 \times 1.5\,\text{mm}^2$ (74×74 viscous units) bins with 50% overlap, while the first window started at the moving plate. It is clear from figure 3(*a*) that the velocity in the vicinity of the wall is detected as high as $u = 0.75\,\text{ms}^{-1}$, which is $u/U_\infty \approx 0.85$ of the wall velocity.

Figure 4 shows the viscous-scaled mean streamwise velocity, $U^+ = U/U_\tau$, against the viscous-scaled wall-normal height, $z^+ = zU_\tau/\nu$ at three streamwise locations of $x = 1.48, 2.30$ and $3.39\,\text{m}$. At these three locations, Re_τ increases as $Re_\tau = 1721, 2092$ and 2444, respectively. As can be seen, the three velocity profiles are shifted downward compared with the log law of a smooth wall turbulent boundary layer, $U^+ = \kappa^{-1}\log z^+ + A$ (shown with dot-dashed lines), where $\kappa \approx 0.386$ is the von Kármán constant and $A \approx 4.17$ is the log intercept for the smooth wall. This shift is expected over rough walls and known as the velocity roughness function, ΔU^+. It is worth noting, that since increases in Re_τ are here achieved with match plate velocities but increasing x location along the plate, ΔU^+ is reduced with Re_τ. The tinted paper technique performs well enabling near rough wall measurements even for this relatively long standoff distance and low magnification setup, where the first detected point is at $z^+ \approx 10.0$.

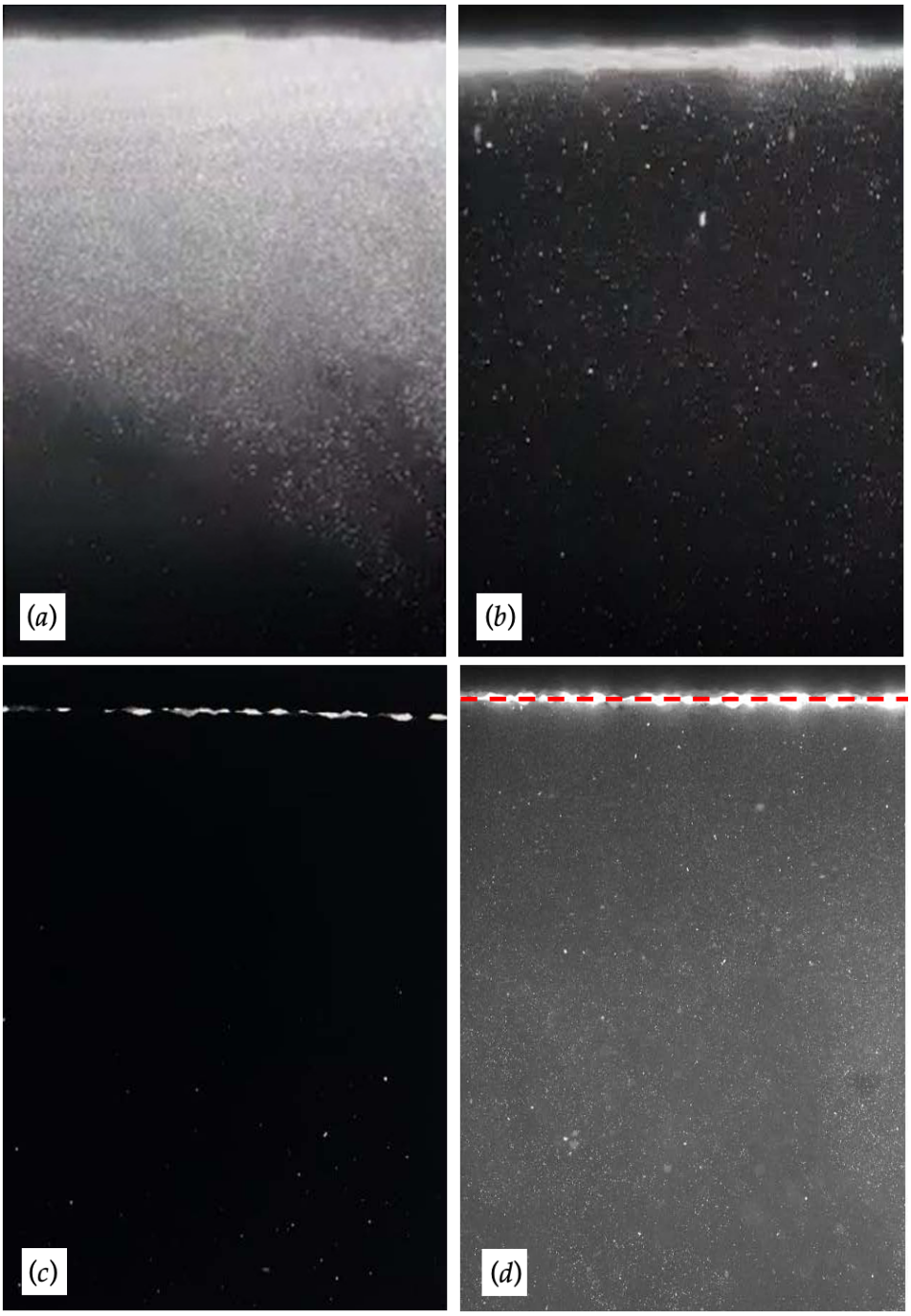

Figure 2. Sample images from the planar-PIV system showing the wall reflection (*a*) without reflection mitigation, (*b*) with one layer of tinted paper covering the FOV, (*c* and *d*) with three layers of tinted paper covering the FOV and covering only the near wall, respectively. The dashed red line in (*d*) shows the edge of the tinted paper as it only covers the upper side of the red dashed line. Note here that all the images have the same colour scale and they are acquired with the same f-stop.

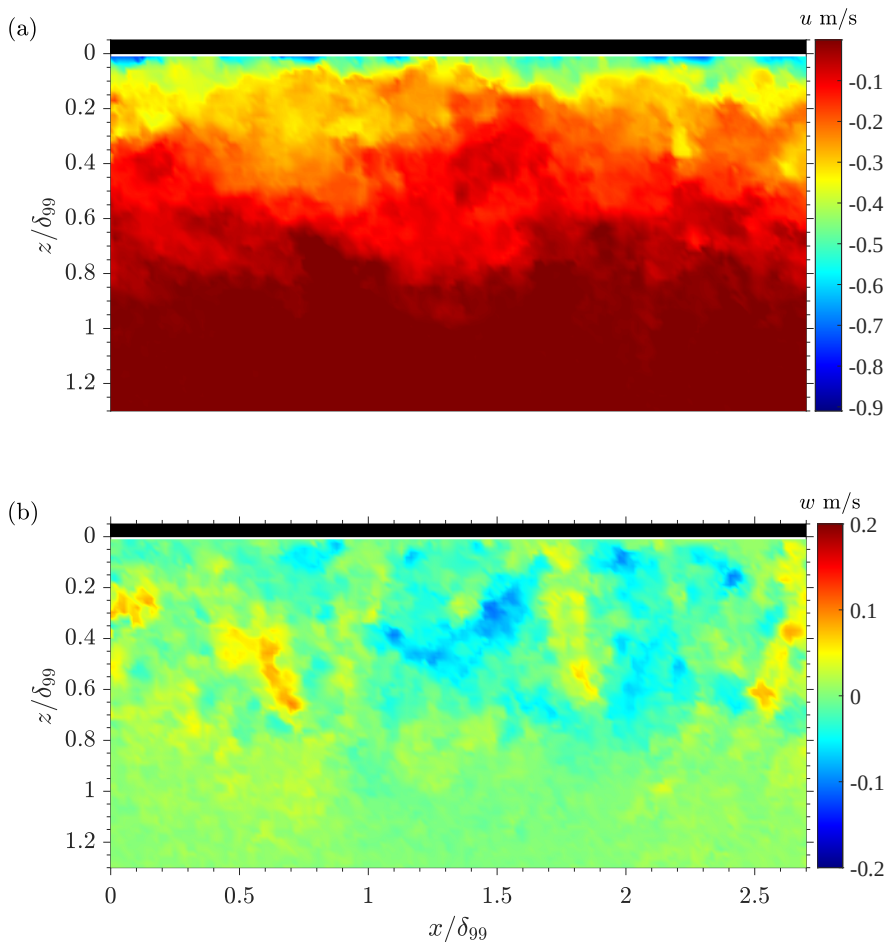

Figure 3. Instantaneous snapshots starting at $x = 1.5$ m of (*a*) streamwise u and (*b*) wall-normal w velocity. The plate is at $z = 0$ mm moving from right-to-left at $U_w = 0.87$ ms^{-1} while the flow is stationary.

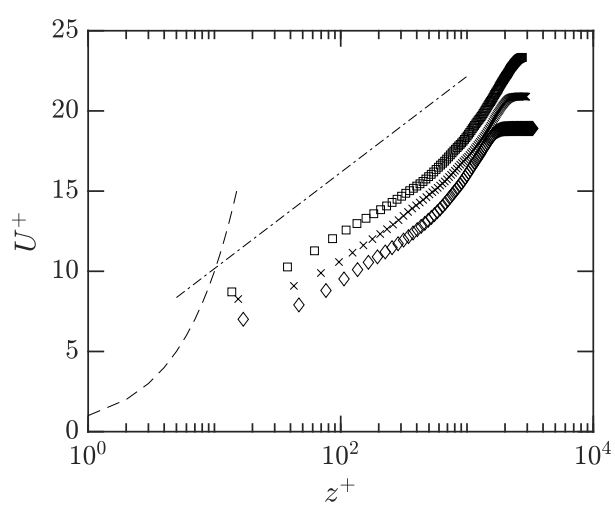

Figure 4. Viscous scaled mean streamwise velocity, U^+ versus the viscous scaled wall-normal distance, z^+. Here $\diamond$ is obtained at $x = 1.48$ m and $Re_\tau = 1721$, $\times$ is at $x = 2.30$ m and $Re_\tau = 2092$ and $\square$ is at $x = 3.39$ m and $Re_\tau = 2444$. The smooth wall law-of-the-wall ($U^+ = z^+$) and the log-law ($U^+ = \kappa^{-1} \log z^+ + A$) are shown with dashed and dot-dashed lines, reflectively.

3. Laser reflection mitigation for stereo-PIV

As shown in the previous section, the masking technique can be used to mitigate the laser reflection of the rough wall for planar PIV measurements. However, this masking technique will not work for air flows seeded with small particles (e.g. ≈ 1 µm polyamide particles) since these particles reflect less light compared with the reflection from the 10 µm silver-coated particles used in the previous section. Then the reflected light from the surface will be much greater than the particle intensities. Also, using the masking technique cannot be used for stereo-PIV since it is not straightforward to mask the prospective view of each camera. For those reasons, we utilise in this section the fluorescent paint technique to shift the reflected light wavelength. Then, a filter for each camera is used to pass only the 532 nm reflected light by the particles. The experimental setup is discussed in section 3.1. Then evaluation of different fluorescent paint is performed in section 3.2, before the results are discussed in section 3.3. Finally, in section 3.4 we perform measurements over drag-increasing trapezoidal riblets using two stereo-PIV systems to provide flow details close to the riblet tips and within the riblet grooves.

3.1. Experimental apparatus and procedures

The measurements are performed in a zero-pressure gradient, open-return wind tunnel facility in the Walter Basset Aerodynamics Laboratory at the University of Melbourne. The working section dimensions are $6.7 \times 0.94 \times 0.38$ m^3 in the streamwise (x), spanwise (y) and wall-normal (z) directions. The tunnel roof and side walls are constructed from clear acrylic and glass, respectively, for clear optical access. A full description of this facility is available in Nugroho et al. (2013).

We use two PCO 4000 cameras with 4008×2672 pixels^2 charge-coupled device (CCD) sensor and a 9.0×9.0 µm^2 pixel size. The two cameras are placed upstream and downstream of the measurement plane on the side of the tunnel with $85°$ between their lines of sight, see figure 5(*a*). Each camera is equipped with a Scheimpflug mount and a Tamron 180 mm macro lens. This optical setup results in FOV1, annotated in blue in figure 5(*a*), is $\Delta y \times \Delta z = 79 \times 52$ mm^2 $(0.97\delta \times 0.64\delta)$ with an effective resolution of 54 µm/pix. The flow is seeded with ≈ 1 µm polyamide particles from a fog generator. These particles are illuminated with a 3.0 mm thickness $y - z$ laser sheet (figure 5 *a*) provided by an InnoLas SpitLight Compact PIV 400 dual pulse Nd: YAG laser. All measurements in this section are obtained at streamwise distance $x = 3.8$ m from the tripwire at the inlet of the working section.

The floor of the tunnel is covered with tiles that have the same random roughness as that used in the 2D-PTV tow tank experiments in section 2.1, shown in figure 1 (*b*). The tunnel is operated at a fixed freestream velocity of 15 ms^{-1}. At this freestream velocity, the root-mean-square viscous-scaled roughness height is $k^+ = kU_\tau/\nu = 64.9$, where $U_\tau = 0.649$ ms^{-1}.

The initial calibration of the cameras is performed using a 3D Calibration target (LaVision GmbH # 1108961) with 5.0 mm space between the dots. The initial distortion of the disparity map is about 1 pixel. The residual RMS is lowered to about 0.02 pixels by applying the self-calibration technique

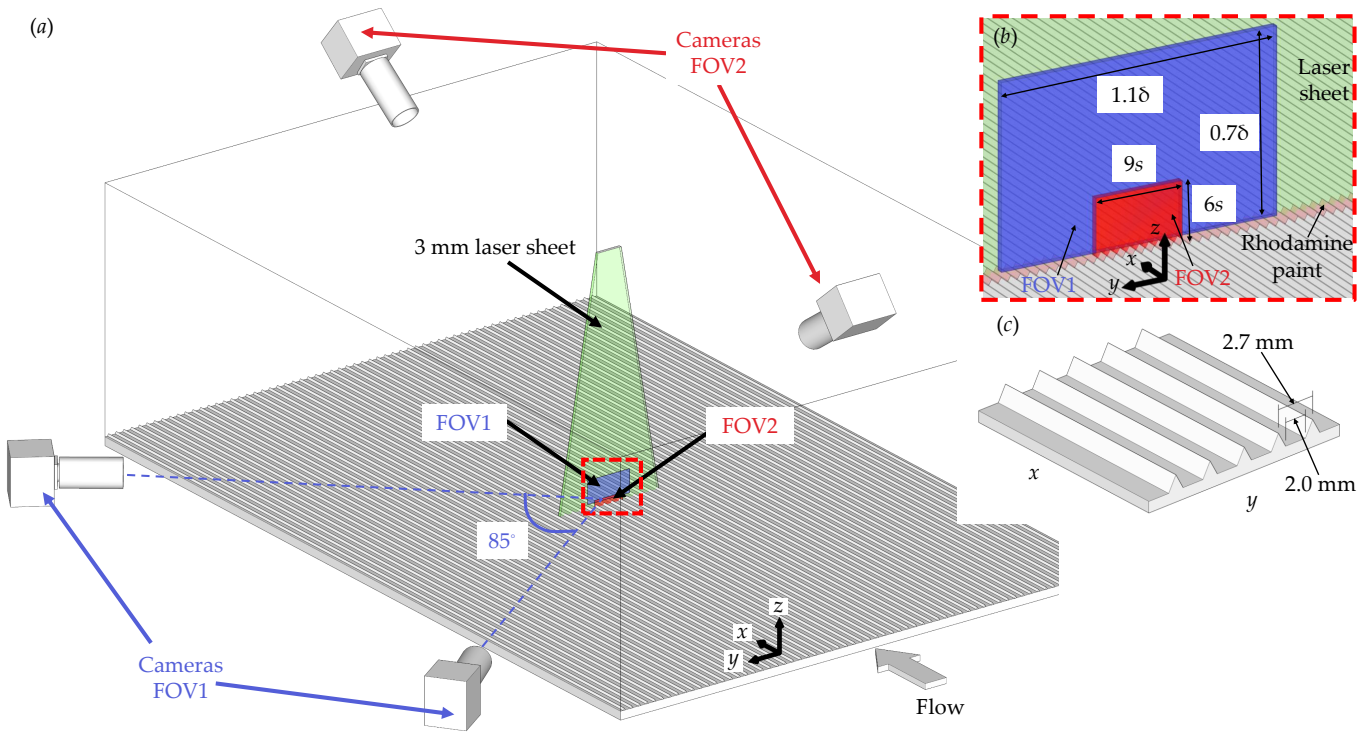

Figure 5. (*a*) Schematic of the stereo-PIV systems on a roughness tile showing the camera arrangement, the $y - z$ laser sheet and the FOV regions. The roughness on the tunnel floor here is scaled up for clear viewing. (*b*) a zoomed view on the FOVs, as indicated by a red dashed line in (*a*), showing the Rhodamine paint and the FOVs location and dimensions, where s is the riblet tip spacing. (*c*) A schematic of the 30° trapezoidal riblet surface used in section 3.4 showing the riblet spacing and orientation.

(Wieneke, 2008). The minimum intensity of the ensemble of images is subtracted from each image, followed by image normalization using the average intensity. Further improvement of the signal-to-noise ratio is sought by normalizing the intensity over a window with a kernel of 10 pixels and a Gaussian smoothing of 3×3 pixels to avoid any peak locking (C. J. Kähler et al., 2012). The improved images are processed with the stereo-PIV algorithm in Davis 10.2 (LaVision GmbH).

A baseline hot-wire measurement is also carried out and located at the tunnel's centre in the spanwise direction. The hot-wire measurement is at the same freestream velocity and streamwise location ($x = 3.8$ m) as that of the stereo-PIV. A modified DANTEC 55P05 probe with 5 µm diameter platinum core Wollaston wire is used. The wire active sensing length is 1 mm, satisfying the recommended 200 length-to-diameter ratio. An in-house Melbourne University constant temperature anemometer (MUCTA) with a 1.8 overheat ratio is used. The probe is traversed in a spanwise and wall-normal grid, with 31 logarithmic spaced wall-normal points, and 11 equally spaced spanwise points spanning 2δ.

3.2. Fluorescent paint evaluation

To have sufficient illumination within the valleys, the laser is directed normal to the roughness ($y-z$ laser sheet), as shown in figure 5. For this reason, there is a strong reflection from the roughness saturating the cameras, as illustrated in the sample image in figure 6. The scattered light from the wall has a higher intensity than the particles and prevents near-surface measurements. To overcome this issue, we tested three types of fluorescent paint for the illuminated surface area of the roughness. These coatings are Kiton Red 620, Dykem Steel Red and Rhodamine 6G. These three coatings have the same fundamental technique of emitting light at a wavelength of 602 nm when illuminated with 532 nm green light. The three types have been used previously to reduce laser reflection of a smooth wall (Depardon et al., 2005; Perce & Lu, 2011; Palmer et al., 2012; Eboibi et al., 2014; Hickling et al., 2019). Dykem Steel Red is supplied as a spray can. In comparison, Kiton Red 620 and Rhodamine 6G are powder-based and prepared with a gram of fluorescent paint, 3 mL methanol and 50 mL polyurethane paint. The mixture results in the optimum consistency to evenly spread over the surface.

For evaluation of the three fluorescent paint types, we use PCO4000 cameras viewing downwards from the tunnel roof at 45° (see camera arrangement for FOV2 in figure 5). For this camera configuration, the camera is more subjected to the direct wall reflection. The camera is equipped with a Scheimpflug mount and a Tamron 180 mm macro lens. A narrow band-pass filter with pass wavelength range of 532 nm ± 5 nm and 95% transmission (Edmund optics, # 65-216) is installed on the camera to extinguish the light reflected by the illuminated surface from the captured images. The reflection evaluation is performed at stationary flow and with no seeding since we are only interested at this point in the scattered light from the wall. The tested roughness for this evaluation is the trapezoidal riblet illustrated in figure 5, since this roughness, among other rough walls, appeared to have the strongest scattered light, see figure 7(*a*). Figure 7(*b*–*d*) show the reflection

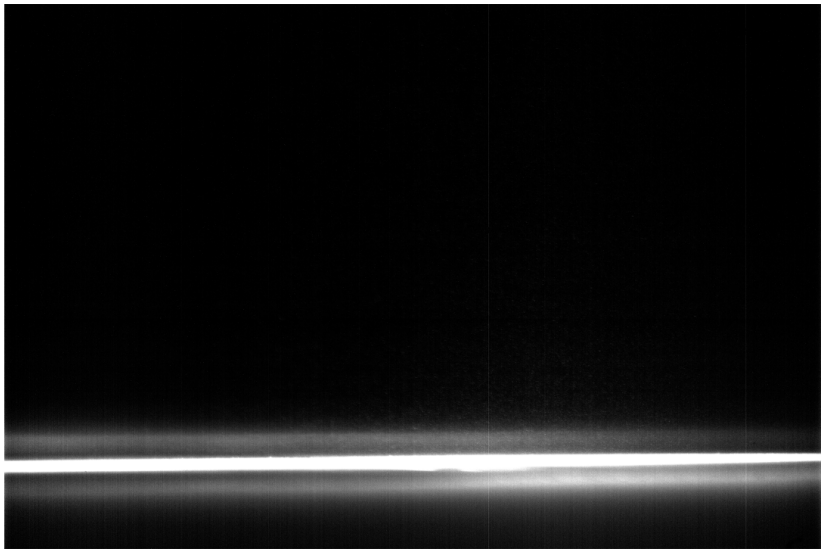

Figure 6. Samples of a raw stereo-PIV image for stationary flow with no seeding over the three-dimensional roughness show the glow from the illuminated roughness in the stereo-PIV.

suppression by each of the painted surfaces. The three fluorescent paints significantly reduced the reflection compared with the uncoated surface in figure 7(*a*). Although Kiton Red 620 helps reduce the saturation of the cameras (see figure 7*b*) and is less hazardous as it does not contain Rhodamine, the region near riblets valleys still saturates the camera at high intensity. The Rhodamine in Dykem Steel Red or Rhodamine 6G appears to give the best results with visibility in the riblet valleys as shown in figure 7(*c* and *d*), respectively, though Rhodamine 6G most effectively suppresses the wall and background reflection. Hereafter in this study, we only use Rhodamine 6G. It is worth noting that the reflection from the wall and the background noise tend to increase over the course of the experiments, presumably due to the build-up of oil from the seeding fog on the surface. Thus, the tile requires periodic cleaning during the experiment with a dry cloth to remove any residuals that might cause reflection and limit the measurement in the vicinity of the wall.

3.3. Results of stereo-PIV over the three-dimensional roughness

Multiple pass cross-correlation is used to process the double-frame stereo-PIV images using DaVis 10.2. The last pass interrogation window is 24×24-pixel ($910 \times 910\,\mu\text{m}^2$). The mean streamwise velocity, U, obtained from averaging the correlated stereo-PIV images in spanwise direction and time is shown in figure 8(*a*) and (*b*) against the wall-normal distance in linear and semi-logarithmic axes, respectively. The mean streamwise velocity profile from the hot-wire is also presented with '$\circ$' in figure 8(*a* and *b*) for comparison. The mean velocity profile of the stereo-PIV shows a good agreement with hot-wire data. The first data point captured by the stereo-PIV is at 500 µm (0.007δ or 5.0 wall units) from the valley of the roughness, which is much closer to the wall compared with the first measured point by the hot-wire probe at (0.6 mm). There is one data point detected within the linear vicious sublayer by the stereo-PIV, and thus estimating the friction velocity, U_τ, by fitting

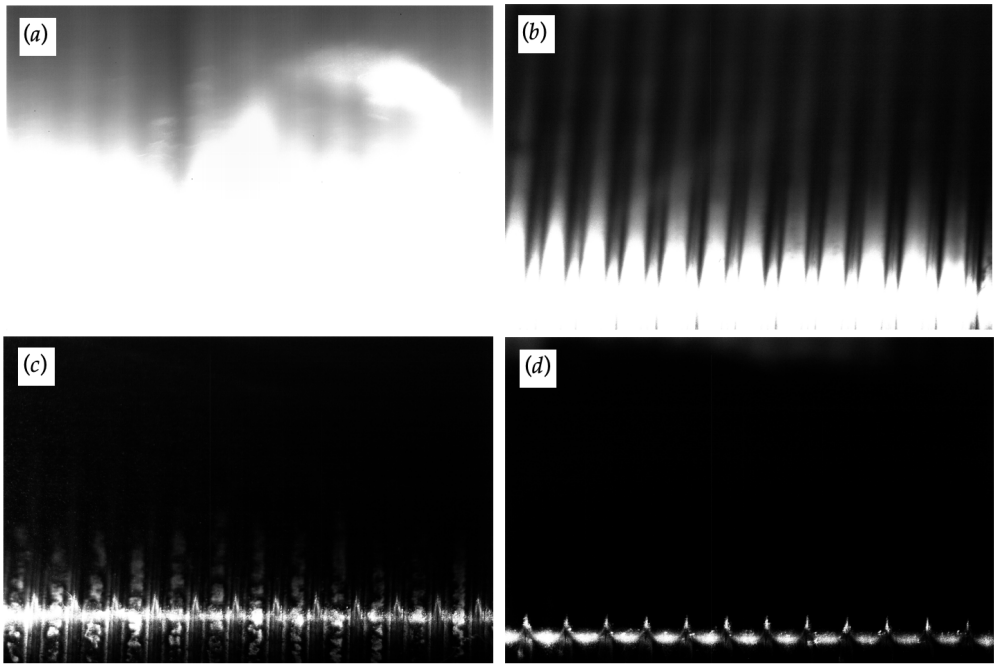

Figure 7. Images over riblet tiles (*a*) non-coated, (*b*) coated Kiton Red 620 (*c*) coated Dykem Steel Red and (*d*) coated Rhodamine 6G obtained from the upstream camera at the roof of the tunnel (FOV2). The images were captured with stationary flow and no seeding particles. Note here that all the images have the same colorscale and they are acquired in the same ambient lighting conditions, and with the same fstop.

a line to the linear viscous sublayer is not applicable in this case. Nonetheless, the fluorescent paint technique enabled velocity measurements in the vicinity of the wall for the stereo-PIV.

The viscous-scaled mean streamwise velocity, U^+, of the stereo-PIV and hot-wire in figure 8(*b*) are normalised with the corresponding U_τ. For both profiles, U_τ is estimated by the modified Clauser chart method. The friction velocity from the both stereo-PIV and hot-wire is comparable at $U_\tau \approx 0.65$. Both profiles are comparable within the error of the set freestream velocity. As shown previously in figure 4, the rough wall shifts U^+ downward compared with the smooth wall log law in figure 8(*b*).

3.4. Stereo-PIV over drag increase riblets

From the stereo-PIV over the rough wall, we found that the fluorescent paint technique could substantially suppress the light reflection from the wall, allowing for velocity measurements in the vicinity of the wall. We further explore the use of this technique for riblet surfaces due to their unsolved mechanism to increase skin friction. Several hypotheses have been proposed to explain the increase in skin friction for oversized riblets. The first hypothesis suggests that beyond a certain size, riblets allow the near-wall streamwise vortices to lodge within the valleys, increasing the wetted area exposed to turbulence and thus increasing the skin friction drag (Choi et al., 1993). The second hypothesis by Goldstein & Tuan (1998) indicates that oversized riblets generate separation or shedding from spanwise turbulent motions above the tips, leading to the formation of time-

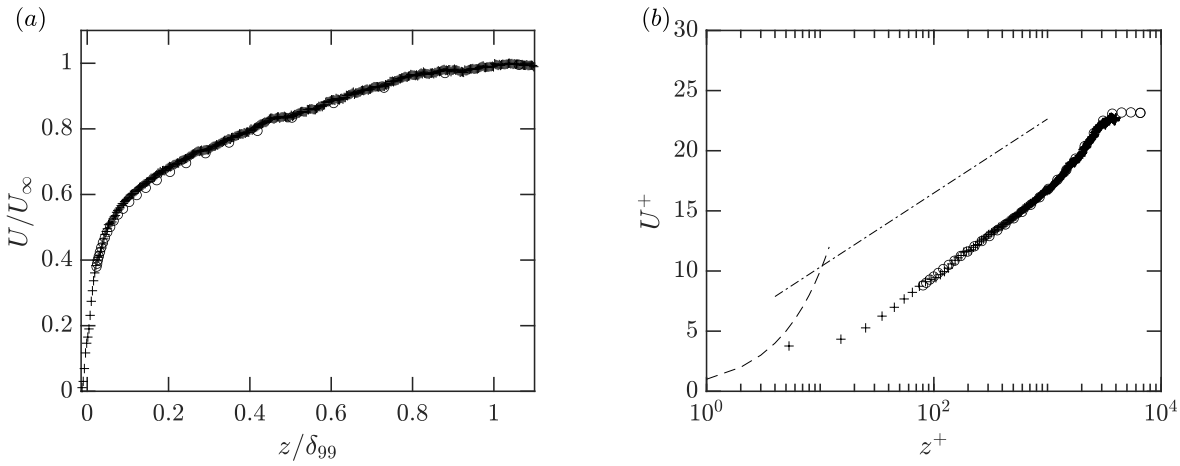

Figure 8. Mean streamwise velocity profiles over the three-dimensional roughness at $x = 3.8$ m plotted in (*a*) linear and (*b*) semi-logarithmic axes. The stereo-PIV results are shown with $+$ while the hot-wire results over the same surface is shown with $\circ$. The smooth wall law-of-the-wall ($U^+ = z^+$) and the log-law ($U^+ = \kappa^{-1} \log z^+ + A$) are shown with dashed and dot-dashed lines, respectively.

mean secondary flows. Garcia-Mayoral & Jimenez (2011) associated the onset of the drag increase of oversized riblets to the existence of Kelvin-Helmholtz instability. Recently, the hot-wire measurements of Newton et al. (2018) show from premultiplied energy spectra that oversized riblets can substantially diminish large-scale energy in the near-wall region. To investigate the proposed hypotheses mentioned above, we use two stereo-PIV systems to perform measurements over drag-increasing trapezoidal riblets. The first system is configured to capture the large-scale turbulent structures above the riblet tips. This system is similar to that used to capture FOV1 over the rough wall in section 3.3 and shown in figure 5(*a*). The second system provides a highly magnified simultaneous view focused on the region close to the riblet tips and within the riblet grooves to quantify the secondary flows. For both of these systems, we use Imperx Bobcat ICL-B6620 cameras with 6600×4400 pixels^2 charge-coupled device (CCD) sensor and a $5.5 \times 5.5\,\mu\text{m}^2$ pixel size. For the first system, when Imperx cameras replace the PCO cameras, the effective resolution for FOV1, becomes 12 µm/pix.

For the second system recording FOV2, we use two cameras placed on the tunnel roof upstream and downstream of the measurement plane (figure 5*a*), each equipped with a Scheimpflug mount, 200 mm Nikon Micro Nikkor and teleconverter $\times 2$. The final magnification and digital resolution are 0.52 and 3.8 µm/pix, respectively. The cameras are angled at $\pm 45^\circ$ with respect to the $x-$direction. The FOV for this system is $\Delta y \times \Delta z = 18 \times 12\,\text{mm}^2$, highlighted in red (FOV2) in figure 5(*b*). The cameras in this system allow for detailed measurements of the flow around the tips of the riblets and within the riblet valleys.

The first 5.5 m of the tunnel floor is covered with trapezoidal riblets constructed from five acetal copolymer tiles. The trapezoidal riblets on each tile, machined in-house with a three-axis CNC router, have 30° tip angle, $s = 2.73$ mm tip spacing and $h = 1.37$ mm base-to-peak height (i.e., $h/s = 0.5$), refer to the schematic shown in figure 5(*c*). These riblets have the same profile as those

studied by Newton et al. (2018). The tunnel is also operated at $U_\infty = 15\,\mathrm{ms}^{-1}$. At this freestream velocity, the viscous-scaled riblet spacing, $s^+ \approx 145$. At this measurement location, the thickness of the boundary layer over the riblet is $\delta \approx 67\,\mathrm{mm}$.

Figure 9 presents samples of raw images of the stereo-PIV FOV1 and FOV2. The particles in figure 9(*a*) are captured very close to the riblet peaks, as also shown in the inset of figure 9(*a*). A thick strip (15 cm) in the *x*-direction of the tile is coated with Rhodamine 6G paint to prevent any glare upstream and downstream of the measurement location, as shown in figure 5(*b*). In the raw images, some reflection may appear in the background of the side cameras due to reflections from tunnel sidewalls. However, this reflection typically has less intensity than the illuminated particles and can be omitted with initial processing steps. Figure 9(*b*) shows a sample raw image from the downstream camera on the tunnel roof. The particles are captured within the valleys of the riblets. The particles density in figure 9(*b*) is kept low since the chosen density must be a compromise between the requirements of FOV1 and FOV2 (which have very different magnifications). There is still a glare where the laser illuminate the valleys of the riblet grooves, limiting the measurement within the valleys to $z \gtrsim 390\,\mu\mathrm{m}$ (21 wall units) from the base of the riblets.

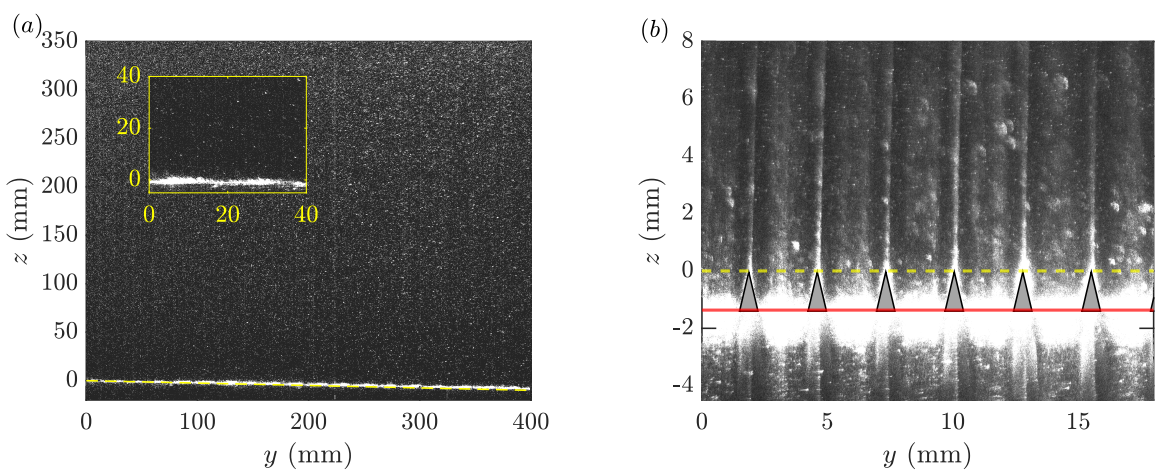

Figure 9. Sample raw images of the simultaneously acquired stereo-PIV of (*a*) FOV1 and (*b*) FOV2. Both images are cropped in width and height for clarity. The yellow dashed line in (*a* and *b*) is at the peaks of the riblets ($z = 0$) while the red solid line in (*b*) is at the valley. The inset in (*a*) shows a close view to riblet peaks.

Preliminary velocity field results of the side cameras stereo-PIV over riblets in figure 10(*a*) show that there are organised lobes above the tips for the spanwise velocity averaged in time $\overline{V}^+ = \overline{V}/U_\tau$. It is clear that those loops are positive on the right tip of the riblets and negative on the left side of the tips, see figure 10(*b*). These lobes are associated with the counter-rotating vortices at the peaks and may extend within the grooves (Modesti et al., 2021).

To track these vortices within the valleys, we also ensemble the velocity of the upper cameras in time. The averaged spanwise velocity $\overline{V}^+$ has four lobes, two at the peaks and two at the valleys, with alternating directions, see figure 11. This a first-time experimental evidence indicate that the oversized riblets generate shedding or break up at the riblet tips, leading to secondary flows within

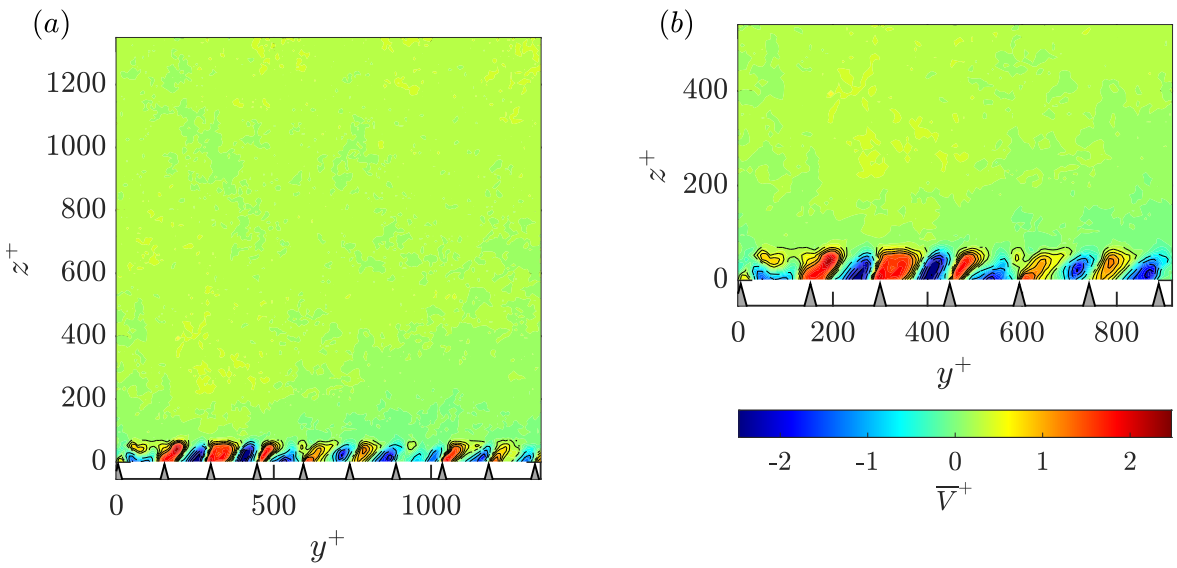

Figure 10. (*a*) Mean spanwise velocity averaged in time $\overline{V}^+$ from the side stereo-PIV FOV1. (*b*) A closer look to the riblet tips. The solid line contour indicates the positive values while the dashed line indicates the negative values. The origin $z^+ = 0$ here is at the riblets tips.

the valleys. With the current experimental ability to measure within the valleys of the riblet, we aim to understand the relation between the large-scale energy above the riblets to the secondary flows within the valleys and will be subject of future analysis.

4. Conclusions

The suppression of light reflection near a rough wall for PIV measurement is investigated in this work. When the use of fluorescent particles is not practical, and the reference rough wall location is required to be present in the images, we provide a technique to control the reflection from a rough wall using layers of tinted paper placed between the cameras and the imaging plane for planar velocity measurements. The tinted paper was positioned to mask only the rough wall to minimise its reflection while keeping the rest of the FOV exposed, allowing the illuminated light from the particles to be captured by the camera sensor. It was found that three layers of 65% light blockage tinted papers were the optimum combination to reduce the wall reflection while keeping minimum glare of the roughness to be detected. These tinted papers reduced the wall reflection while keeping minimum glare of the roughness to be detected. This technique showed a substantial improvement to the velocity results in the vicinity of the rough wall, allowing for velocity measurements at ~ 300 µm from the wall for the low magnification (< 0.2) imaging system.

The wall reflection was also reduced for stereo-PIV measurements using fluorescent paint on the roughness while band-pass filters were attached to the cameras. The current results show that the fluorescent paints containing Rhodamine suppress the majority of wall reflections compared with Kiton Red 620. Rhodamine 6G paint and band-pass filters for the cameras allowed velocity mea-

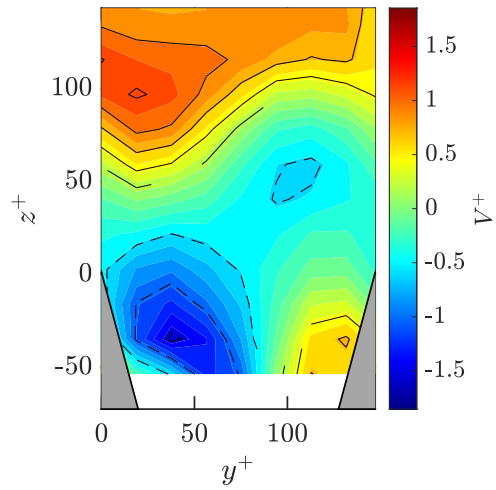

Figure 11. Mean spanwise velocity averaged in time and over riblet periods V^+ from the top stereo-PIV FOV2. The solid line contour indicates the positive values while the dashed line indicates the negative values. The origin $z^+ = 0$ here is at the riblets tips.

surements above the roughness tips and within the valleys. These successful preliminary results pave the way for further analysis which will be aimed at characterising the secondary flows above riblets and within their valley.

Acknowledgements

This work is supported by the Air Force Office of Scientific Research under award number FA2386-21-1-4018 (program managers: Ryan Carr and Doug Smith) and also the Australian Research Council Discovery Project DP200102824.

Nomenclature

U_τ	Friction velocity [ms^{-1}]
ν	Kinematic viscosity [m^{2}s^{-1}]
k	Roughness height [m]
s	Riblet spacing [m]
h	Riblet height [m]
Re	Reynolds number
x	Streamwise direction [m]
U	Streamwise velocity [ms^{-1}]
y	Spanwise direction [m]
z	Wall-normal direction [m]

References

Abu Rowin, W., Hou, J., & Ghaemi, S. (2017). Inner and outer layer turbulence over a superhydrophobic surface with low roughness level at low reynolds number. *Physics of Fluids*, *29*(9), 095106.

Bhatia, J. C., Durst, F., & Jovanovic, J. (1982). Corrections of hot-wire anemometer measurements near walls. *Journal of Fluid Mechanics*, *122*, 411–431.

Choi, H., Moin, P., & Kim, J. (1993). Direct numerical simulation of turbulent flow over riblets. *Journal of Fluid Mechanics*, *255*, 503–539.

Depardon, S., Lasserre, J., Boueilh, J., Brizzi, L., & Borée, J. (2005). Skin friction pattern analysis using near-wall piv. *Experiments in Fluids*, *39*(5), 805–818.

Dreyer, M., Decaix, J., Münch-Alligné, C., & Farhat, M. (2014). Mind the gap: a new insight into the tip leakage vortex using stereo-piv. *Experiments in Fluids*, *55*(11), 1–13.

Eboibi, O., Edwards, J., Howell, R., & Danao, L. A. (2014). Development of velocity flow field measurement method around a vertical axis wind turbine blade using particle image velocimetry. In *Proceedings of the world congress on engineering* (Vol. 2).

Garcia-Mayoral, R., & Jimenez, J. (2011). Hydrodynamic stability and breakdown of the viscous regime over riblets. *Journal of Fluid Mechanics*, *678*, 317–347.

Goldstein, D., & Tuan, T.-C. (1998). Secondary flow induced by riblets. *Journal of Fluid Mechanics*, *363*, 115–151.

Gui, L. (1997). Evaluation of low image density recordings with the mqd method and application to the flow in a liquid bridge. *Journal of Flow Visualization & Image Processing*, *4*, 333–343.

Hickling, C., Balantrapu, N. A., Alexander, W. N., Millican, A. J., Devenport, W. J., & Glegg, S. A. (2019). Turbulence ingestion into a rotor at the rear of an axisymmetric body. In *25th aiaa/ceas aeroacoustics conference* (p. 2571).

Jelly, T. O., & Busse, A. (2019). Multi-scale anisotropic rough surface algorithm: Technical documentation and user guide.

Kähler, C. (2009). High resolution measurements by long-range micro-piv. *Proceedings of VKI Lecture Series on Recent Advances in Particle Image Velocimetry*.

Kähler, C. J., Scharnowski, S., & Cierpka, C. (2012). On the uncertainty of digital piv and ptv near walls. *Experiments in Fluids*, *52*(6), 1641–1656.

Khoo, B. C., Chew, Y., & Teo, C. (2000). On near-wall hot-wire measurements. *Experiments in Fluids*, *29*(5), 448–460.

Meinhart, C. D., Wereley, S. T., & Santiago, J. G. (1999). Piv measurements of a microchannel flow. *Experiments in Fluids*, *27*(5), 414–419.

Modesti, D., Endrikat, S., Hutchins, N., & Chung, D. (2021). Dispersive stresses in turbulent flow over riblets. *Journal of Fluid Mechanics*, *917*.

Newton, R., Chung, D., & Hutchins, N. (2018). An experimental investigation into the breakdown of riblet drag reduction at post-optimal conditions. In *21st australasian fluid mechanics conference, adelaide, australia.*

Nugroho, B., Hutchins, N., & Monty, J. P. (2013). Large-scale spanwise periodicity in a turbulent boundary layer induced by highly ordered and directional surface roughness. *International Journal of Heat and Fluid Flow*, *41*, 90–102.

Palmer, J. A., Mejia-Alvarez, R., Best, J. L., & Christensen, K. T. (2012). Particle-image velocimetry measurements of flow over interacting barchan dunes. *Experiments in Fluids*, *52*(3), 809–829.

Perce, A., & Lu, F. (2011). New seeding and surface treatment methods for particle image velocimetry. In *49th AIAA aerospace sciences meeting including the new horizons forum and aerospace exposition* (p. 1164).

Rothstein, J. P. (2010). Slip on superhydrophobic surfaces. *Annual review of fluid mechanics*, *42*, 89–109.

Rowin, W. A., & Ghaemi, S. (2019). Streamwise and spanwise slip over a superhydrophobic surface. *Journal of Fluid Mechanics*, *870*, 1127–1157.

Talapatra, S., & Katz, J. (2012). Coherent structures in the inner part of a rough-wall channel flow resolved using holographic piv. *Journal of Fluid Mechanics*, *711*, 161–170.

Vanderwel, C., & Ganapathisubramani, B. (2015). Effects of spanwise spacing on large-scale secondary flows in rough-wall turbulent boundary layers. *Journal of Fluid Mechanics*, *774*.

Wangsawijaya, D. D., Baidya, R., Chung, D., Marusic, I., & Hutchins, N. (2020). The effect of spanwise wavelength of surface heterogeneity on turbulent secondary flows. *Journal of Fluid Mechanics*, *894*.

Wereley, S. T., Gui, L., & Meinhart, C. (2002). Advanced algorithms for microscale particle image velocimetry. *AIAA journal*, *40*(6), 1047–1055.

Wieneke, B. (2008). Volume self-calibration for 3d particle image velocimetry. *Experiments in Fluids*, *45*(4), 549–556.